Transfer coefficients for evaporation of a system with a Lennard-Jones long-range spline potential

Jialin Ge, S. Kjelstrup,* D. Bedeaux, and J. M. Simon†
Department of Chemistry, Norwegian University of Science and Technology, NO-7491 Trondheim, Norway

B. Rousseau
Laboratoire de Chimie Physique, Bâtiment 349, CNRS UMR8000, Université Paris-Sud, 91405 Orsay Cedex, France
(Received 15 December 2006; revised manuscript received 30 March 2007; published 21 June 2007)

Surface transfer coefficients are determined by nonequilibrium molecular dynamics simulations for a Lennard-Jones fluid with a long-range spline potential. In earlier work [A. Røsjorde *et al.*, J. Colloid Interface Sci. **240**, 355 (2001); J. Xu *et al.*, *ibid.* **299**, 452 (2006)], using a short-range Lennard-Jones spline potential, it was found that the resistivity coefficients to heat and mass transfer agreed rather well with the values predicted by kinetic theory. For the long-range Lennard-Jones spline potential considered in this paper we find significant discrepancies from the values predicted by kinetic theory. In particular the coupling coefficient, and as a consequence the heat of transfer on the vapor side of the surface are much larger. Thermodynamic data for the liquid-vapor equilibrium confirmed the law of corresponding states for the surface, when it is described as an autonomous system. The importance of these findings for modelling phase transitions is discussed.

DOI: 10.1103/PhysRevE.75.061604 PACS number(s): 68.03.−g, 45.50.Jf

I. INTRODUCTION

Phase transitions are common in nature as well as in industry. So the study of the transport properties of the surface between two phases is very important. A phase transition involves simultaneous transfer of heat and mass across a surface, and large efforts have been devoted to model this in a correct way [3]. Many of these studies have assumed equilibrium between the phases at the phase boundary, i.e., continuity in the chemical potential(s) and the temperature. In such a case, the resistivities of the surface to heat and mass transfer play no role.

We have questioned this assumption for liquid-vapor phase transitions [4,5,2], not because we find very large resistivities for this transition [2,6,1], but because the coupling of heat and mass at the surface is important. The coupling coefficient measures how much of the enthalpy of evaporation is taken from each of the adjacent phases [4]. Therefore, the coupling coefficient will influence the value of the heat fluxes into the homogeneous phases. So it is important to know its value and understand its origin. Linear kinetic theory (KT) [7] has since long, predicted the transfer coefficients for the surface, also the coupling coefficient, and given explicit formulas for them. Kinetic theory applies to particles that are hard spheres, however. In lack of information on real systems, the surface resistivities for heat and mass transfer have mostly been neglected in the engineering description of phase transitions. Experiments have been done, which confirm the presence of a temperature difference across the liquid-vapor interface. In experiments the problem becomes at least two dimensional. Phenomena like convection may occur. We refer to Duan *et al.* [8] and references therein. For a detailed analysis of the various theoretical descriptions and their application to the experiments we refer to Bond and Struchtrup [9].

This work aims to add to the understanding of the surface resistivities, and in particular to give information about the coefficient that describes coupling of heat and mass. We shall find all transfer coefficients by applying the nonequilibrium molecular dynamics simulation technique (NEMD) to a system with a long-range Lennard-Jones spline potential, and compare the results to kinetic theory as well as to results obtained earlier with a short-range Lennard-Jones spline potential [1,2]. The long-range potential is a better approximation to the real Lennard-Jones potential than its short-range version. We want to know whether the good agreement with kinetic theory obtained earlier [2] is accidental or not, and in general to contribute to the systematic knowledge of these coefficients.

In a study of transport properties of surfaces, one first must establish the surface boundaries, and the equilibrium properties of the surface. This shall be done also here. One needs to establish the proper equation of state, before one can calculate thermodynamic driving forces in the system. The surface and its equilibrium thermodynamic properties have been defined here following Gibbs [10].

In the description of the transfer coefficients, we use nonequilibrium thermodynamics theory, as developed for surfaces [4]. The basic hypothesis of nonequilibrium thermodynamics is the hypothesis of local equilibrium. When the surface is defined as a separate system, as mentioned above, one must verify that the equation of state for the surface applies equally well in the presence as in the absence of gradients across the surface. This was done earlier, working with Lennard-Jones spline particles [11,1] and with *n*-octane [6]. In both cases the systems were exposed to a large temperature gradient. We shall see that the assumption is true also here, meaning that classical nonequilibrium thermodynamics can be used.

*Corresponding author.
†On leave from Institute Carnot de Bourgogne, UMR 5209 CNRS-Universit de Bourgogne, F-21078 Dijon, France.

In a system with longer interacting potentials, we therefore want to answer the following main questions: Is the surface still in local equilibrium in a temperature gradient? How will the transfer resistivities vary with the range of the potential? Can kinetic theory predict the correct results in this case? While the answer to the first question is yes, as we shall see, the changes are such that the answer to the last question is no. We furthermore shall show that the surface obeys the law of corresponding states also in the presence of a large temperature gradient.

II. NONEQUILIBRIUM THERMODYNAMICS FOR THE SURFACE

The primary quantity of a nonequilibrium system is its entropy production. This quantity governs the equations of transport. For a surface, nonequilibrim thermodynamics gives the equations of transport from the excess entropy production. For a surface in a stationary state, the excess entropy production rate with heat and mass transport into and through the surface is [12]

$$\sigma^s = J_q'^g\left(\frac{1}{T^s}-\frac{1}{T^g}\right)+J_q'^l\left(\frac{1}{T^l}-\frac{1}{T^s}\right)-J\left(\frac{\mu^l(T^s)-\mu^g(T^s)}{T^s}\right). \tag{1}$$

Here $J_q'^g$ is the measurable heat flux from the gas into the surface and $J_q'^l$ is the measurable heat flux out of the surface into the liquid. J is the mass flux across the surface, which is constant in a stationary state. According to the hypothesis of local equilibrium, the surface is a separate thermodynamic system and has its own temperature T^s. The temperature next to the surface on the liquid side is T^l and on the gas side it is T^g [4,5]. The chemical potential next to the surface on the liquid side is μ^l and on the gas side it is μ^g. The positive direction is defined as being from the vapor to the liquid. The notation follows de Groot and Mazur [13] and Bedeaux and Kjelstrup [4]. In a stationary state, the total heat flux through the surface is constant,

$$J_q = J_q'^l + H^l J = J_q'^g + H^g J. \tag{2}$$

It follows that

$$J_q'^l = J_q'^g + J\Delta_{\mathrm{vap}}H. \tag{3}$$

Here H is the molar enthalpy and $\Delta_{\mathrm{vap}}H=H^g(T^g)-H^l(T^l)$ is the heat of evaporation. Using this relation to eliminate the term containing $J_q'^l$ in the excess entropy production, and noticing the thermodynamic identity

$$\frac{\mu(T^l)}{T^l}-\frac{\mu(T^s)}{T^s}=H\left(\frac{1}{T^l}-\frac{1}{T^s}\right) \tag{4}$$

both for the vapor and the liquid, we can reduce the excess entropy production to

$$\sigma^s = J_q'^g\left(\frac{1}{T^l}-\frac{1}{T^g}\right)-J\frac{1}{T^l}[\mu^l(T^l)-\mu^g(T^l)] = J_q'^g X_q + JX_\mu^g. \tag{5}$$

In Eq. (4) the enthalpy can be taken at T^g, T^s or T^l to linear order in the differences. If one uses the measurable heat flux in the liquid as a variable, we obtain the alternative expression

$$\sigma^s = J_q'^l X_q + JX_\mu^l. \tag{6}$$

In the above equations, X_q, X_μ^g, and X_μ^l are the thermal driving force and chemical driving forces, respectively,

$$X_q = \Delta\left(\frac{1}{T}\right)=\frac{1}{T^l}-\frac{1}{T^g},$$

$$X_\mu^g = -\frac{1}{T^l}\Delta\mu_T(T^l) = -\frac{1}{T^l}[\mu^l(T^l)-\mu^g(T^l)],$$

$$X_\mu^l = -\frac{1}{T^g}\Delta\mu_T(T^g) = -\frac{1}{T^g}[\mu^l(T^g)-\mu^g(T^g)]. \tag{7}$$

According to classical nonequilibrium thermodynamics, the thermodynamic forces are linear combinations of their conjugate fluxes

$$X_q = r_{qq}^{s,g}J_q'^g + r_{q\mu}^{s,g}J,$$

$$X_\mu^g = r_{\mu q}^{s,g}J_q'^g + r_{\mu\mu}^{s,g}J. \tag{8}$$

Here the coefficients $r_{qq}^{s,g}$ and $r_{\mu\mu}^{s,g}$ are the two main resistivities of the surface. They are for heat transfer and mass transfer, respectively. The coefficients $r_{q\mu}^{s,g}$ and $r_{\mu q}^{s,g}$ are the coupling resistivities. They describe the mass transport due to the temperature difference and the heat transport due to the mass flux, respectively. According to the Onsager reciprocal relations $r_{q\mu}^{s,g}=r_{\mu q}^{s,g}$. The above equations (8) are appropriate when the measurable heat flux on the gas side is used. In the same way we obtain equations which use the measurable heat flux on the liquid side:

$$X_q = r_{qq}^{s,l}J_q'^l + r_{q\mu}^{s,l}J,$$

$$X_\mu^l = r_{\mu q}^{s,l}J_q'^l + r_{\mu\mu}^{s,l}J. \tag{9}$$

The two sets of equations are equivalent. The resistivities of the two sets are related by

$$r_{qq}^{s,l} = r_{qq}^{s,g},$$

$$r_{q\mu}^{s,l} = r_{\mu q}^{s,l} = r_{q\mu}^{s,g} - \Delta_{\mathrm{vap}}Hr_{qq}^{s,g},$$

$$r_{\mu\mu}^{s,l} = r_{\mu\mu}^{s,g} - 2\Delta_{\mathrm{vap}}Hr_{\mu q}^{s,g} + (\Delta_{\mathrm{vap}}H)^2 r_{qq}^{s,g}. \tag{10}$$

The interface film resistivities from kinetic theory were discussed by Xu *et al.* [2]. The authors proposed that the surface temperature be used in the expressions obtained from Cipolla *et al.* [7], rather than the liquid temperature. This gave a better fit to the simulation data. Also it is more appropriate that a property of the surface depends on the temperature of the surface. The revised expressions, proposed by Xu *et al.*, were

$$r_{qq}^{s,g}(T^s) = \frac{1.27640}{R(T^s)^2 c^g(T^s)}\sqrt{\frac{M}{3RT^s}},$$

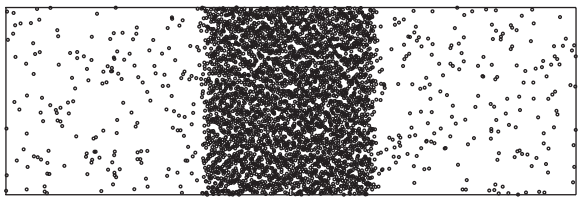

FIG. 1. A snapshot of the MD box with 4096 particles. The axes are not drawn with the same scale, see text for aspect ratio.

$$r_{\mu q}^{s,g}(T^s) = r_{q\mu}^{s,g}(T^s) = \frac{0.54715}{T^s c^g(T^s)} \sqrt{\frac{M}{3RT^s}},$$

$$r_{\mu\mu}^{s,g}(T^s) = \frac{4.34161R(\sigma_c^{-1}(T^s) - 0.39856)}{c^g(T^s)} \sqrt{\frac{M}{3RT^s}}. \quad (11)$$

Here $c^g(T^s)$ is the density of a vapor in equilibrium with a liquid at the temperature of the surface, M is the molar mass, and R is the gas constant. The condensation coefficient, σ_c, gives the fraction of particles that condense at the surface after collision with the liquid. Values between 0.1 to 1.0 have been reported [14] for this coefficient.

III. MOLECULAR SIMULATION METHOD

A. Simulation system

The nonequilibrium molecular dynamics simulation (NEMD) method was described in more detail elsewhere [2]. Here we briefly describe its main aspects. The simulation box, is a noncubic, rectangular one, with length ratios $L_x/L_y = L_x/L_z = 16$. Here L_i is the length of the box in the ith direction. We simulated 4096 argonlike particles. Periodic boundary conditions were used. Normally the size of the box was about 10 molecular diameters (10σ) in the direction along the surface and about 160 molecular diameters (160σ) in the direction normal to the surface, the x direction. The NEMD simulations were done with a constant number of particles N and volume V. In equilibrium the thermostatted regions were thermostatted to the same temperature. This produced a canonical ensemble. Different overall densities of the model system were obtained by varying the size of the box. The densities were chosen such that the mean free path in the vapor was smaller than the thickness of the vapor layer in the direction normal to the surface. The mean free path was calculated using the standard formula $l = 1/(\sigma^2 c N_A \pi\sqrt{2})$. For two out of three simulations the mean free path was larger than (up to 10 times) the length of the box in the direction parallel to the surface. In view of the fact that we calculate resistivities for transport normal to the surface this is not expected to be a problem. No behavior of the data indicated such an effect. The simulation box was divided in the x direction into 128 equal planar layers parallel to the surface. A snapshot of the system, which clearly shows the vapor and the liquid phases, is given in Fig. 1.

In order to create a temperature gradient, the layers at the end of the box, layers 1–2 and 127–128, which we called the hot zones, were thermostatted to a high temperature T_H, and the layers in the center of the box, layers 63–66, called the cold zone, were thermostatted to a low temperature T_L. This is done by the "heat exchange" (HEX) algorithm [15], which adds or withdraws energy in these layers. In this way, a heat flux from the ends of the box to the center was created.

TABLE I. Reduced units.

Variable	Reduction formula
Mass	$m^* = m/m_1$
Distance	$r^* = r/\sigma$
Energy	$U^* = U/\varepsilon$
Time	$t^* = (t/\sigma)\sqrt{\varepsilon/m_1}$
Temperature	$T^* = kT/\varepsilon$
Density	$c^* = c\sigma^3 N_A$
Pressure	$p^* = p\sigma^3/\varepsilon$
Velocity	$v^* = v\sqrt{m_1/\varepsilon}$
Surface tension	$\gamma^* = \gamma\sigma^2/\varepsilon$

We simulated a mass flow using the "mass exchange" (MEX) algorithm [15], which moves particles from the cold zone to the hot zone. This is done by randomly selecting a particle in the cold zone and changing its location up or down by half a box length. It was then verified that the particle at its new location had no overlap with any of the particles already present. In the case of overlap the move was rejected.

To calculate the driving forces, the equilibrium properties were necessary. The equilibrium properties of the system, were studied by equilibrium molecular dynamics (EMD) simulations and some Gibbs ensemble Monte Carlo (GEMC) simulations [16]. To obtain the equilibrium phase diagram by molecular dynamics, we performed simulations on the above system. We first run the code for 1 million time steps at nonequilibrium states with the cold zone thermostatted at a lower temperature and the hot zone at a higher temperature. Every time step was 0.0005 in reduced units (see Table I). This created an interface in the cell. Then we set the high temperature equal to the low temperature and run the code for 5 million time steps at the appropriate equilibrium state. This gave the density and pressure of vapor and liquid in coexistence. GEMC simulations at constant volume, temperature, and total number of particles allow for direct simulation of phase equilibria in a pure component without an explicit interface. Two cubic simulation boxes were simulated and thermal, mechanical, and chemical equilibrium between both phases were obtained by means of Monte Carlo moves, including particle translation, volume changes (at constant total volume), and particle transfer between phases. Starting from an initial configuration, equilibrium was reached and the density of both phases and the vapor pressure were obtained.

B. Potential

A Lennard-Jones spline potential was used to describe the particle interaction. The potential is expressed in terms of the interparticle distance r_{ij} between any pair of particles i and j,

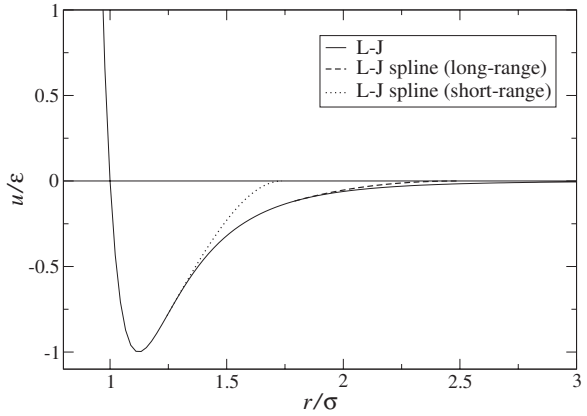

FIG. 2. The Lennard-Jones potential, the short- and the long-range Lennard-Jones spline potentials.

$$u(r_{ij}) = \begin{cases} 4\varepsilon[(\sigma/r_{ij})^{12} - (\sigma/r_{ij})^{6}], & 0 < r_{ij} < r_s, \\ a(r_{ij} - r_c)^2 + b(r_{ij} - r_c)^3, & r_s < r_{ij} < r_c, \\ 0, & r_c < r_{ij}, \end{cases} \quad (12)$$

where $r_c = 2.5\sigma$ is the truncated distance and $r_s = (48/67)r_c$. The constants a and b were chosen so that the potential and its derivative are continuous at r_s. In r_c the potential and its derivative are also continuous. In the simulations, we used argonlike particles with mass $m_1 = 6.64 \times 10^{-26}$ kg, diameter $\sigma = 3.42 \times 10^{-10}$ m, and the potential depth $\varepsilon/k = 124$ K. Here k is Boltzmann's constant. This resulted in $a = 0.099\,194$ J/m^2 and $b = -0.163\,46$ J/m^3. Plots of the Lennard-Jones potential and the short- and the long-range Lennard-Jones spline potentials are given in Fig. 2.

Reduced units in terms of potential parameters were used for all variables in the computer codes, see Table I for definitions.

C. Case studies

GEMC simulations were performed in order to obtain the critical coordinates of the long-range Lennard-Jones spline potential. A set of 14 simulations at reduced temperatures ranging from 0.9 to 1.3 were realized. For each simulation, we used a total number of 500 particles. Probability attempts for the different moves were 0.88 for translation, 0.1 for transfer, and 0.02 for volume change. All simulations ran for 21 million Monte Carlo steps and average properties were computed from the last 18 million steps.

We performed 20 nonequilibrium molecular dynamics simulations in the study of the transport properties of the surface, see Table II. Every simulation ran 10 million time steps with a time step of 5×10^{-4} in reduced units, which is equivalent to about 10^{-15} s in real time. The first 3 million time steps were abandoned to avoid transient effects. All the properties were averaged over 7 million time steps. Because the system is symmetric about the central plane in the middle of the box in a stationary state, in the x direction, the mean of the properties in each half-box was furthermore calculated to obtain better statistics. The density in the vapor phase is very low. Accuracy of the values calculated for the vapor phase is obtained by running the stationary state simulations long enough.

TABLE II. NEMD simulation conditions, in reduced and real units.

Simulation	c^*	T_H^*	T_N^*	J^*	c (mol/m^3)	T_H (K)	T_L (K)	J (mol/m^2 s)
1	0.20	1.10	0.75	0.001	8302	136.4	93.0	6666
2	0.20	1.10	0.70	0.001	8302	136.4	86.8	6666
3	0.30	1.20	0.65	0.002	12453	148.8	80.6	13332
4	0.23	1.25	0.85	0.002	9547	155.0	105.4	13332
5	0.23	1.30	0.90	0.002	9547	161.2	111.6	13332
6	0.23	1.35	0.95	0.002	9547	167.4	117.8	13332
7	0.23	1.40	1.00	0.002	9547	173.6	124.0	13332
8	0.23	1.20	0.80	0.002	9547	148.8	99.2	13332
9	0.23	1.15	0.75	0.002	9547	142.6	93.0	13332
10	0.23	1.10	0.70	0.002	9547	136.4	86.8	13332
11	0.15	1.10	0.60	0	6226	136.4	74.4	0
12	0.20	1.10	0.60	0	8302	136.4	74.4	0
13	0.20	1.10	0.75	0	8302	136.4	93.0	0
14	0.23	1.25	0.85	0	9547	155.0	105.4	0
15	0.23	1.30	0.90	0	9547	161.2	111.6	0
16	0.23	1.35	0.95	0	9547	167.4	117.8	0
17	0.23	1.40	1.00	0	9547	173.6	124.0	0
18	0.23	1.20	0.80	0	9547	148.8	99.2	0
19	0.23	1.15	0.75	0	9547	142.6	93.0	0
20	0.23	1.10	0.70	0	9547	136.4	86.8	0

Among the 20 NEMD simulations for the surface transfer coefficients, 10 had a mass flux, and the other 10 did not (see Table II). We chose a suitably high temperature, low temperature, and overall density so that two vapor-liquid surfaces appeared in the box. The temperature gradients went beyond usual laboratory values. They were of the order of 10^9 K/m in the vapor and 10^8 K/m in the liquid.

D. Defining the surface

The extension of the surface is an issue of discussion. On the gas side, a good equation of state is available. This is the Soave-Redlich-Kwong (SRK) equation [17].

$$p = \frac{RT}{v-b} - \frac{a}{v(v+b)}, \tag{13}$$

where the coefficients were found to be given by [11,2]

$$a = 0.427\,48\frac{R^2T_c^2}{p_c}\left[1 + 0.4866\left(1 - \sqrt{\frac{T}{T_c}}\right)\right]^2,$$

$$b = 0.086\,64\frac{RT_c}{p_c}. \tag{14}$$

From knowledge of the critical coordinates $T_c = 138.9 \pm 0.1$ K and $p_c = 4.25 \times 10^6$ Pa (obtained by GEMC) the gas phase molar volume v and molar density $\rho = 1/v$ can be computed as a function of pressure and temperature by solving the SRK equation. In each layer this density was compared with the one obtained from NEMD. For the pressure in this calculation it is appropriate to use the volume average of the pressure normal to the surface, see below. A layer is defined as a interfacial layer when these densities differ seriously.

On the liquid side, we do not have an equation of state to help us determine the first layer of the surface. But the transition from liquid to the surface is rather abrupt. From the liquid layer to the surface layer, the density changes markedly. As the first surface layer we took the layer next to the last layer on the liquid side with a density that is still equal to the liquid density. The interfaces were found to be roughly 10 layers thick. Given this thickness, there was no indication that the interface was not perfectly flat.

The results reported refer to this choice. We have earlier found that the exclusion and/or inclusion of one extra layer does not alter the results significantly [1].

E. Calculations

The fluxes and thermodynamic properties of each layer were calculated as time averages using instantaneous velocities, kinetic energies, potential energies, and the number of particles. The molar density in layer ν ($\nu = 1, 2, \ldots, 128$) was given by

$$c_\nu = \frac{128 N_\nu}{V N_A} \tag{15}$$

here N_ν is the number of particles in layer ν and $V = L_x L_y L_z$ is the volume of the system. The molar flux in layer ν was

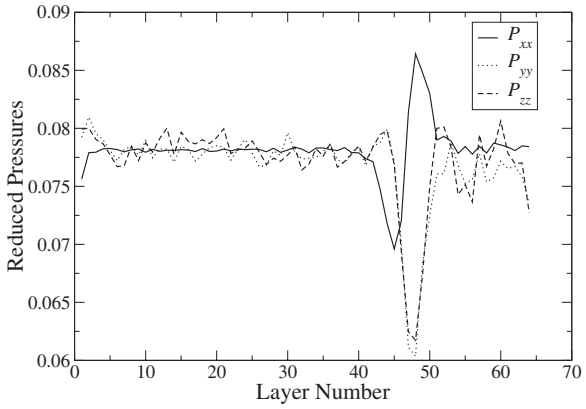

FIG. 3. The reduced diagonal pressures for simulation 7 as a function of layer number.

$$\mathbf{J}_\nu = c_\nu \mathbf{v}_\nu = \frac{c_\nu}{N_\nu} \sum_{i \in \nu} \mathbf{v}_i, \tag{16}$$

where $\mathbf{v}_\nu$ is the velocity of the center of mass in layer ν. In the stationary state considered only the x component of the molar flux and the barycentric velocity, J_ν and v_ν, are unequal to zero.

The temperature in each layer was found from the particles' kinetic energy

$$\frac{3}{2} N_\nu k T_\nu = \frac{1}{2} \sum_{i \in \nu} m |\mathbf{v}_i - \mathbf{v}_\nu|^2. \tag{17}$$

The temperatures T^g and T^l were chosen to be equal to the temperatures of the last layers of the vapor and the liquid next to the surface layers. These then give the thermal force X_q. For the temperature of the surface we used the value which is found from the kinetic energy of the surface layers. In terms of the temperatures of the layers that are part of the surface this gives

$$T^s = \sum_{\nu \in \text{surface}} N_\nu T_\nu \Big/ \sum_{\kappa \in \text{surface}} N_\kappa. \tag{18}$$

The local pressure tensor was calculated by time averaging the microscopic pressure tensor

$$p^\nu_{\alpha\beta} = \frac{128}{V} \sum_{i \in \nu} \left(m v_{i,\alpha} v_{i,\beta} + \frac{1}{2} \sum_{j \neq i} F_{ij,\alpha} r_{ij,\beta} \right), \tag{19}$$

where $v_{i,\alpha}$ is the velocity of particle i in the direction α, $F_{ij,\alpha}$ is the force exerted on particle i by particle j in the direction α, and $r_{ij,\beta}$ is the component of the vector from particle j to particle i in the direction β. The pressure tensor was found to be diagonal. Away from the surface the diagonal elements in the x, y, and z directions are the same. In the neighborhood of the surface it is found that the diagonal elements along the surface, $p_\parallel = p_{yy} = p_{zz}$, and normal to the surface, $p_\perp = p_{xx}$, are different. In Fig. 3 we plot the diagonal elements of the reduced pressure tensor for simulation 7. In the work by Todd *et al.* [18,19] it is shown that the method of planes is a more efficient procedure to calculate the pressure tensor when the system is inhomogeneous. They consider in particular fluids

under shear conditions and with large or varying density gradients. In this paper there is no shear, the density gradient is smaller and smooth. Away from the interface we find the expressions given to be appropriate. In the interfacial region the method of planes leads to a normal pressure which is closer to being constant as it should be [6]. As we did not further need this information, we did not pursue this further.

The surface tension was computed from

$$\gamma = \frac{1}{A}\sum_{i<j}(r_{ij} - 3x_{ij}^2/r_{ij})u'(r_{ij}), \tag{20}$$

where $A = L_y L_z$ is the surface area of the cross section in the y and z directions. The x direction is the direction normal to the surface, and $x_{ij} = x_i - x_j$, while $u'(r_{ij})$ is the derivative of the pair potential with respect to interparticle distance, r_{ij}. Equation (20) gives the surface tension of one of the two surfaces by restricting the particles to be either in layers 3–62 or in 67–126. If the sum is not restricted in this manner one must divide by $2A$.

The total heat flux $\mathbf{J}_q$ is constant while the measurable heat flux $\mathbf{J}_q'$ varies due to the temperature dependence of the enthalpy per mole H. The total heat flux is

$$\mathbf{J}_q = \mathbf{J}_q' + H\mathbf{J}. \tag{21}$$

The total heat flux in layer ν is calculated from

$$\begin{aligned}\mathbf{J}_{q,\nu} &= \frac{128}{V}\sum_{i\in\text{layer }\nu}\left[\mathbf{v}_i\left(\frac{1}{2}mv_i^2 + \phi_i\right)\right. \\ &\quad \left. + \mathbf{v}_i\cdot\left(m\mathbf{v}_i\mathbf{v}_i + \frac{1}{2}\sum_{j\neq i}\mathbf{F}_{ij}\mathbf{r}_{ij}\right)\right] \\ &= \frac{128}{V}\sum_{i\in\text{layer }\nu}\left[\mathbf{v}_i\left(\frac{3}{2}mv_i^2 + \phi_i\right) + \frac{1}{2}\sum_{j\neq i}\mathbf{v}_i\cdot\mathbf{F}_{ij}\mathbf{r}_{ij}\right],\end{aligned} \tag{22}$$

where the potential energy of particle i is

$$\phi_i \equiv \frac{1}{2}\sum_j u(r_{ij}). \tag{23}$$

In the stationary state considered only the x component of the total heat flux, $J_{q,\nu}$, is unequal to zero. In Figure 4 we plot the total and the measurable heat flux for simulation 7. In the work by Todd *et al.* [18,19] it is shown that the method of planes is also a more efficient procedure to calculate the heat flux when the system is inhomogeneous. They consider in particular fluids under shear conditions. In the work of this paper there are no shear gradients and we find the expressions given to be appropriate also through the interfacial region. The enthalpy per mole in layer ν is found from

$$H_\nu = \frac{1}{N_A}\left[\frac{5}{2}k_B T_\nu N_\nu + \sum_{i\in\text{layer }\nu}\left(\phi_i + \frac{1}{6}\sum_j \mathbf{F}_{ij}\cdot\mathbf{r}_{ij}\right)\right]. \tag{24}$$

To calculate the chemical driving forces, we use the following formulas [2]:

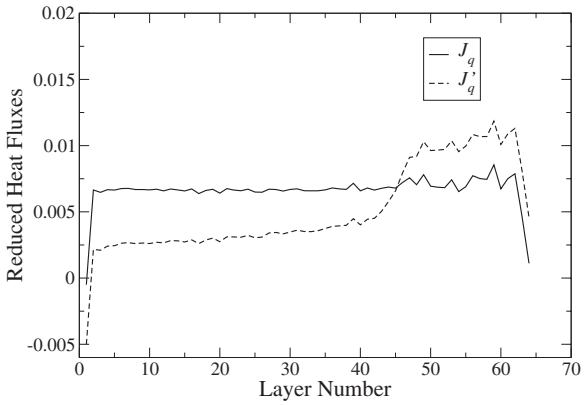

FIG. 4. The reduced heat fluxes for simulation 7 as a function of the layer number.

$$\begin{aligned}X_\mu^g &= R\ln\frac{p}{p^*(T^l)} + R\ln\frac{\phi(T^l,p)}{\phi^*(T^l,p)} + \frac{v^{l*}(T^l)}{T^l}[p^*(T^l) - p] \\ &\quad + \frac{1}{2}c_p^g(T^g)\left(1 - \frac{T^g}{T^l}\right)^2,\end{aligned} \tag{25}$$

$$\begin{aligned}X_\mu^l &= R\ln\frac{p}{p^*(T^g)} + R\ln\frac{\phi(T^g,p)}{\phi^*(T^g,p)} + \frac{v^{l*}(T^g)}{T^g}[p^*(T^g) - p] \\ &\quad + \frac{1}{2}c_p^l(T^l)\left(1 - \frac{T^l}{T^g}\right)^2.\end{aligned} \tag{26}$$

These formulas are valid to second order in the temperature difference. The input quantities are the system pressure, p, saturation pressure, p^*, heat capacities at constant pressure, c_p^g and c_p^l, the liquid molar volume at saturation, v^{l*}. The fugacity coefficient ϕ was obtained using the following formula:

$$\begin{aligned}RT\ln\phi(T,v) &= RT\left(\frac{b}{v-b} + \ln\frac{v}{v-b} - \ln\frac{vp(T,v)}{RT}\right) \\ &\quad - \frac{a}{v+b} + \frac{a}{b}\ln\frac{v}{v+b},\end{aligned} \tag{27}$$

here T, v, p are related by the SRK equation (13).

IV. RESULTS AND DISCUSSION

A. The vapor and liquid at equilibrium

Equilibrium properties are needed for the calculation of the driving forces. The equilibrium properties are also important in themselves, as this particular system has not been studied before. The Lennard-Jones spline potential in this study has a cutoff distance equal to 2.5 reduced units, while 1.73 reduced units were used earlier. Equilibrium results were found with two simulation techniques: The Monte Carlo simulation and the equilibrium molecular dynamics.

Figure 5 shows the vapor-liquid coexistence curve with results from both studies. The reduced density is plotted as a function of the reduced temperature for the two phases. The points at higher temperatures (triangle symbols) are the re-

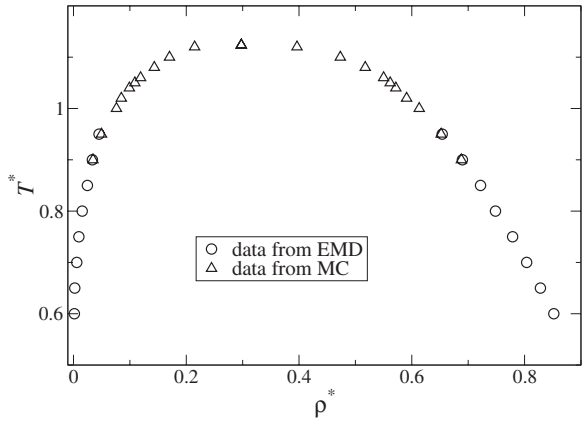

FIG. 5. The liquid-vapor coexistence curve for the Lennard-Jones fluid with a long-range spline potential.

sults of the Monte Carlo simulations. Those at lower temperatures (circle symbols) are from the results of the molecular dynamics simulations. We see that the sets of data agree within some percent in the region where they overlap. The coexistence curve data were fitted by the following formula:

$$\rho_L - \rho_V = \rho_0 \left(\frac{T_c - T}{T_c} \right)^{\beta}. \tag{28}$$

The universal exponent is given by $\beta=0.32$. Furthermore ρ_0 is a system-dependent constant for which we found $\rho_0 = 1.08 \pm 0.02$ in reduced units. The critical temperature was found to be $T_c = 138.9 \pm 0.1$ K.

Figure 6 gives the (reduced) vapor pressure of the system, as a function of the (reduced) temperature. To find a fit to this plot, we used the Clausius-Clapeyron equation:

$$p^*(T) = p_0^* \exp\left(- \frac{\Delta_{\text{vap}} H}{RT} \right), \tag{29}$$

where p_0^* is a constant for which we found $p_0^* = 27 \pm 2$. Furthermore $\Delta_{\text{vap}} H$ is the enthalpy of evaporation. Approximating $\Delta_{\text{vap}} H$ to be constant, we found $\Delta_{\text{vap}} H = 6490 \pm 80$ J/mol. For the short-range spline potential the values were found to be $p_0^* = 18.4$ and $\Delta_{\text{vap}} H = 5205$ J/mol [11].

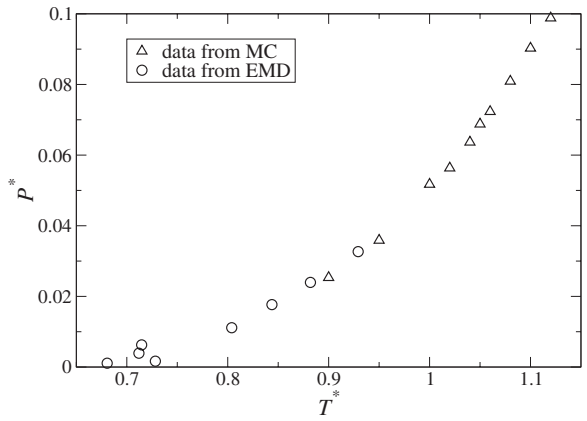

FIG. 6. The vapor pressure as a function of temperature for the Lennard-Jones fluid with a long-range spline potential.

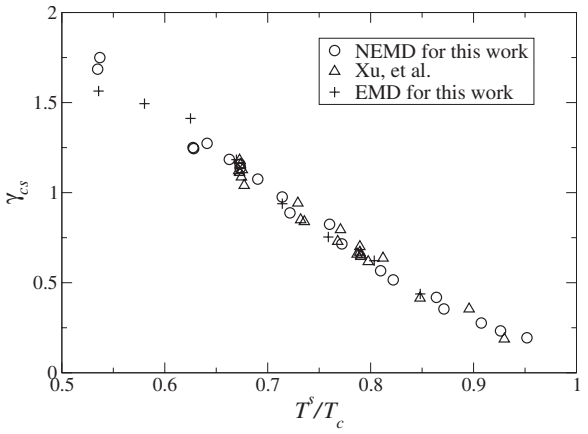

FIG. 7. The equation of state for the liquid-vapor surface for a fluid with a long-range spline potential; the surface tension as a function of temperature at equilibrium (EMD) and at nonequilibrium (NEMD). Results for a short-range spline potential are also shown [2].

The simulations gave a critical temperature $T_c = 138.9$ K, a critical density $\rho_c = 1.235 \times 10^4$ mol/m^3, and a critical pressure $p_c = 4.25 \times 10^6$ Pa. These values are closer to the values of real argon, $T_c = 150.7$ K and $p_c = 4.86 \times 10^6$ Pa, than those obtained for the short-range potential, where we found $T_c = 111.2$ K, and $p_c = 3.32 \times 10^6$ Pa, respectively.

The relationship between the surface tension and the surface temperature is the equation of state for the surface. Following Guggenheim [20,21], we plotted in Fig. 7 the quantity $\gamma_{\text{CS}} = \gamma / (\rho_c^{2/3} k T_c)$ versus $T_{\text{CS}} = T^s / T_c$. These variables were derived from the law of corresponding states and must be distinguished from the reduced surface tension and temperature in Table I. The plot shows the corresponding states surface tension versus corresponding states surface temperature. The circle symbols are from nonequilibrium molecular dynamics simulations (NEMD) and the plus symbols are from equilibrium molecular dynamics simulations (EMD). We can see that they agree well. This proved again [11,6] that the surface is a separate thermodynamic system, which is in local equilibrium, even in the presence of a large temperature gradient. This is the condition for using nonequilibrium thermodynamics. The results from the system with the short-range spline potential [2] are shown in the figure using triangles. The system with a short-range potential have a critical temperature, T_c, and density, ρ_c, that differ considerably from the values given above. By plotting the results in CS units, the results from the earlier investigation agreed with our data. This shows that the principle of corresponding state for the surface tension can be applied successfully to Lennard-Jones spline systems for both short- and long-range potentials.

The data for the surface tension were fitted to the equation of state for the surface

$$\gamma = \gamma_0 \left(\frac{T_c - T}{T_c} \right)^{\nu}, \tag{30}$$

where $\nu = 1.26$ is a universal constant. We obtained $\gamma_0 = 0.0334 \pm 0.0003$ N/m. The value of the constant for the

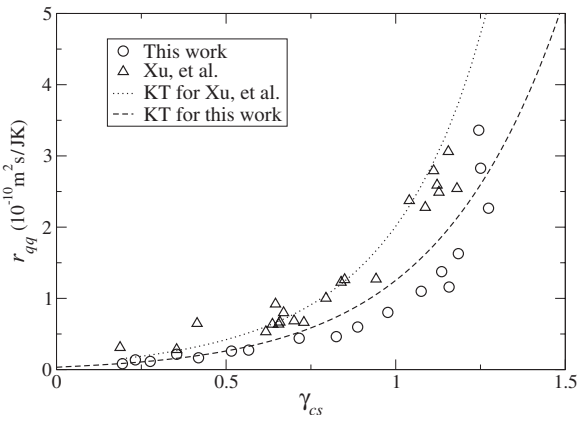

FIG. 8. The surface transfer resistivity r_{qq} to heat flux for a Lennard-Jones system with a long-range spline potential (circles) and for a short-range spline potential (triangles) [2]. Results from KT are also shown for both systems.

short-range potential was $\gamma_0=0.0248\pm0.0003$ N/m. The surface entropy is minus the derivative of the surface tension with respect to the temperature. This gives

$$s^s = \delta_0\left(\frac{T_c - T}{T_c}\right)^{\nu-1}, \tag{31}$$

where $\delta_0=\nu\gamma_0/T_c=3.0\times10^{-4}$ J/m^2. In our earlier paper [2] we found $\delta_0=2.8\times10^{-4}$ J/m^2 for the short-range spline potential.

B. Surface resistivities

Figures 8–12 give plots of resistivities for the equivalent sets of variables, when the measurable heat flux refers to the vapor side (Figs. 8, 9, and 11) and to the liquid side (Figs. 8, 10, and 12). All coefficients were plotted as a function of corresponding states surface tension $\gamma_{CS}=\gamma/(\rho_c^{2/3}kT_c)$. Earlier results [2], and results calculated from kinetic theory using Eq. (11) for both sets of data, are also shown, for comparison.

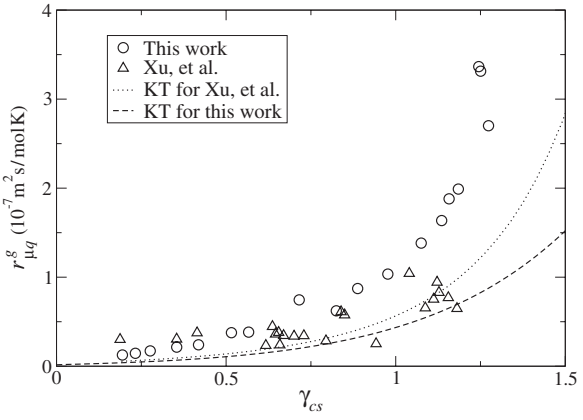

FIG. 9. The surface transfer resistivity $r^g_{\mu q}$ for coupling of the mass flux to the heat flux on the vapor side. Results are shown for a Lennard-Jones system with a long-range spline potential (○) and for a short-range spline potential (△) [2]. Results from KT are also shown for both systems.

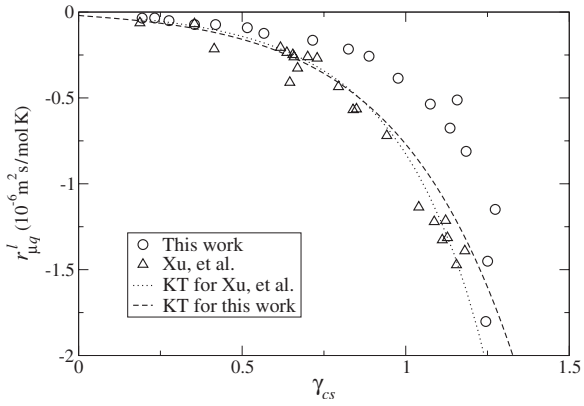

FIG. 10. The surface transfer resistivity $r^l_{\mu q}$ for coupling of the mass flux to the heat flux on the liquid side. Results are shown for a Lennard-Jones system with a long-range spline potential (circles) and for a short-range spline potential (triangles) [2]. Results from KT are also shown for both systems.

Figure 8 shows the main resistivity to heat transfer. This coefficient is the same, whether we use the measurable heat flux on the liquid side or on the vapor side as the flux, cf. Eq. (10a). The results obtained here (the circles) were somewhat smaller than predicted by kinetic theory (the stippled line). For the system with the short-range potential [2], given here by the triangles and the dotted line, the agreement with kinetic theory was better.

Figure 9 shows the coupling resistivity, $r^g_{\mu q}$, for coupling of the mass flux to the measurable heat flux on the vapor side. The values are now a factor of 3 larger than the values predicted by kinetic theory (the stippled line). For the short-range potential, triangles and a dotted line, there was again agreement between the NEMD results and kinetic theory. The absolute value of the coupling resistivities on the liquid side are about 10 times larger than the value of $r^g_{\mu q}$, see Fig. 10. Equation (10b) gives the relation between the coupling coefficients on both sides of the surface. Figure 10 shows that the coupling resistivity $r^l_{\mu q}$ is also affected by a change in the range of the potential. The NEMD values (the circles)

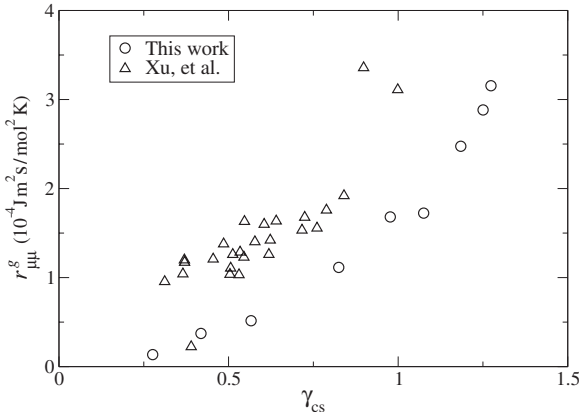

FIG. 11. The surface transfer resistivity $r^g_{\mu\mu}$ to a mass flux when the heat flux on the vapor side is used as a variable, for a Lennard-Jones system with a long-range pline potential (circles) and for a short-range spline potential (triangles) [2].

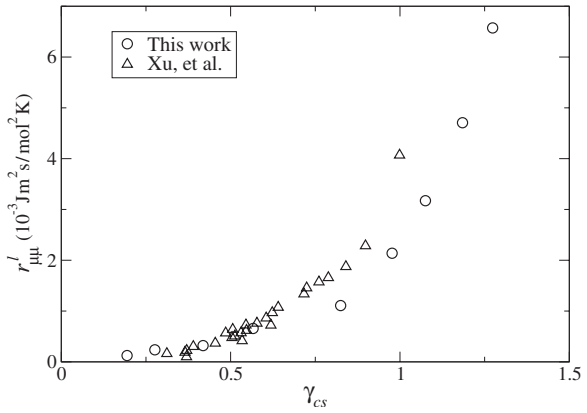

FIG. 12. The surface transfer resistivity $r^l_{\mu\mu}$ to a mass flux when the heat flux on the liquid side is used as variable, for a Lennard-Jones system with a long-range spline potential (circles) and for a short-range spline potential (triangles) [2].

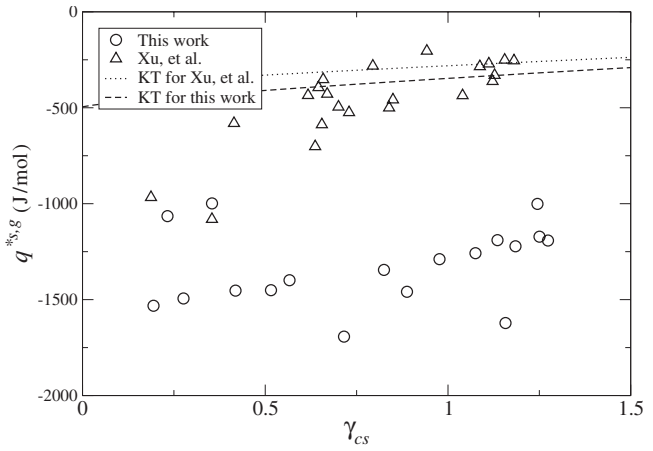

FIG. 13. The heat transfer to the heat flux on the vapor side for the Lennard-Jones fluid with a long-range spline potential (circles) and a short-range spline potential (triangles).

are considerably less negative than the prediction by kinetic theory (the stippled line). For the short-range potential there was agreement between the NEMD values (triangle) and the kinetic theory prediction (dotted line). We conclude therefore that kinetic theory predicts results for the short-range potential well, but it fails to predict the values obtained with the long-range potential. For the long-range potential the coupling resistivities on the vapor side are much larger than the prediction from kinetic theory.

Figures 11 and 12 give the two alternative mass transfer resistivities $r^g_{\mu\mu}$ and $r^l_{\mu\mu}$. Again $r^g_{\mu\mu}$ is small compared to $r^l_{\mu\mu}$. The results for the liquid side have a better accuracy. For the short-range potential, for which the agreement with kinetic theory was so good, we used the mass transfer resistivity to obtain the condensation coefficient. For the long-range potential there is no such agreement and it is therefore not appropriate to obtain a condensation coefficient in this manner.

All resistivities approach zero for zero surface tension close to the critical point as they should. Away from the critical point the resistivities increase their value as the surface tension increases. They all go to a maximum at the triple point. The triple point has the lowest temperature of the investigation.

The nature of the interaction potential has an impact on all system properties, including the equilibrium properties. It is therefore difficult to compare directly the results for the short- and the long-range potential. As kinetic theory accounts for differences in temperature and vapor concentration, we have chosen to discuss the size of two of the coefficients in comparison with this theory. We have then seen that a more realistic potential, the long-range potential, gives a heat transfer resistivity which is slightly smaller than the prediction by kinetic theory and a coupling resistivity which is 3 times larger than the prediction by kinetic theory. This is a substantial difference. This might have been expected, as kinetic theory is developed for hard spheres. A Lennard-Jones fluid with long-range potential therefore agrees even less than the fluid with a short-range potential with the premises of kinetic theory.

C. The heat of transfer

The coupling coefficient for heat and mass transport deserves extra attention, because of its importance to predict the heat flux into the two phases adjacent to the surface. For a physical interpretation, the coupling coefficient is most conveniently expressed via the heat of transfer. When the heat flux on the vapor side is used to define the heat of transfer, we have

$$q^{*s,g} = \left(\frac{J'^g_q}{J}\right)_{\Delta T=0} = -\frac{r^{s,g}_{\mu q}}{r^{s,g}_{qq}}. \tag{32}$$

Using the heat flux on the liquid side, we have

$$q^{*s,l} = \left(\frac{J'^l_q}{J}\right)_{\Delta T=0} = -\frac{r^{s,l}_{\mu q}}{r^{s,l}_{qq}}, \tag{33}$$

where we note that $r^{s,g}_{qq} = r^{s,l}_{qq}$. When these definitions are combined with Eq. (10b), we find

$$q^{*s,l} - q^{*s,g} = \Delta_{\text{vap}} H. \tag{34}$$

During evaporation, there is a heat sink in the surface, given by the enthalpy needed to transfer a particle from the liquid to the vapor phase. The surface may cool down, but at stationary state the heat must come from the surroundings. The heats of transfers give the fractions of the enthalpy of evaporation which must be taken from the respective phases. A large value for say $q^{*s,l}$ means that a large part of the required heat is taken from or returned to the liquid side, depending on the sign of the mass flux. Their absolute ratio $|q^{*s,l}/q^{*s,g}|$ is equal to $|r^{s,l}_{\mu q}/r^{s,g}_{\mu q}|$ and the coupling resistivities are given in Figs. 7 and 8. We find that the absolute value of the heat of transfer is larger on the liquid side than on the vapor side, for the long-range potential (3 times) as well as for the short-range potential (9 times) [2]. So the liquid provides 75% of the required heat for evaporation of particles with a long-range potential and 90% for a short-range potential. The minus sign of the heat of transfer on the vapor side (see Fig. 13) expresses that heat is transferred in a direction opposite to the mass flux.

The heat of transfer on the vapor side from this simulation and from the previous results were compared with the prediction of kinetic theory in Fig. 13. We see again, that the system with the long-range potential is not at all predicted by the corresponding kinetic theory coefficients. For the short-range interaction potential the agreement is reasonable.

V. CONCLUSION

We have used molecular dynamics simulations to study a one-component fluid interacting with a long-range Lennard-Jones spline potential, $r_c=2.5\sigma$. We presented equilibrium properties of the system, and transfer coefficients for heat and mass transport. We found that the relationship between surface tension and surface temperature are the same in equilibrium and in nonequilibrium. This once more proved that, the surface can be regarded a separate system and that this system is in local equilibrium. This is a prerequisite for using nonequilibrium thermodynamics. We calculated the film resistivities and compared them with the values obtained for the short-range potential systems and with kinetic theory. While the predictions of kinetic theory seemed to agree with the results obtained for the short-range potential, they do not agree with our results. For the long-range potential the coupling coefficient on the vapor side was 3 times larger than the prediction by kinetic theory, and cannot be neglected in an accurate calculation of the heat fluxes in the system. This points to a need for more realistic data for transfer resistivities, so that such systems can be accurately modeled.

ACKNOWLEDGMENT

The authors are grateful for the Storforsk Grant No. 167336/V30 from the Norwegian Research Council.

[1] A. Røsjorde, S. Kjelstrup, D. Bedeaux, and B. Hafskjold, J. Colloid Interface Sci. **240**, 355 (2001).
[2] J. Xu, S. Kjelstrup, D. Bedeaux, A. Røsjorde, and L. Rekvig, J. Colloid Interface Sci. **299**, 452 (2006).
[3] R. Taylor and R. Krishna, *Multicomponent Mass Transfer* (Wiley, New York, 1993).
[4] D. Bedeaux and S. Kjelstrup, Int. J. Thermodyn. **8**, 25 (2005).
[5] E. Johannessen and D. Bedeaux, Physica A **330**, 354 (2003).
[6] J. M. Simon, S. Kjelstrup, D. Bedeaux, and B. Hafskjold, J. Phys. Chem. B **108**, 7186 (2004).
[7] J. W. Cipolla, Jr., H. Lang, and S. K. Loyalka, J. Chem. Phys. **61**, 69 (1974).
[8] F. Duan, V. K. Badam, F. Durst, and C. Ward, Phys. Rev. E **72**, 056303 (2005).
[9] M. Bond and H. Struchtrup, Phys. Rev. E **70**, 061605 (2004).
[10] J. W. Gibbs, *The Scientific Papers of J. W. Gibbs* (Dover, New York, 1961).
[11] A. Røsjorde, D. W. Fossmo, D. Bedeaux, S. Kjelstrup, and B. Hafskjold, J. Colloid Interface Sci. **232**, 178 (2000).
[12] D. Bedeaux and S. Kjelstrup, Physica A **270**, 413 (1999).
[13] S. R. de Groot and P. Mazur, *Non-Equilibrium Thermodynamics* (Dover, London, 1984).
[14] T. Ytrehus, Multiphase Sci. Technol. **9**, 205 (1997).
[15] B. Hafskjold and S. K. Ratkje, J. Stat. Phys. **78**, 463 (1995).
[16] A. Z. Panagiotopoulos, Mol. Phys. **62**, 701 (1987).
[17] R. C. Reid, J. M. Prausnitz, and T. K. Sherwood, *The Properties of Gases and Liquids* (McGraw-Hill, New York, 1977).
[18] B. D. Todd, P. J. Daivis, and D. J. Evans, Phys. Rev. E **51**, 4362 (1995).
[19] B. D. Todd, D. J. Evans, and P. J. Daivis, Phys. Rev. E **52**, 1627 (1995).
[20] E. A. Guggenheim, J. Chem. Phys. **13**, 253 (1945).
[21] Volker C. Weiss and Wolffram Schroer, J. Chem. Phys. **122**, 084705 (2005).